JOURNAL OF GEOPHYSICAL RESEARCH, VOL. 117, B01308, doi:10.1029/2011JB008595, 2012

Estimating near-surface shear wave velocities in Japan by applying seismic interferometry to KiK-net data

N. Nakata[1,2] and R. Snieder[2]

Received 16 June 2011; revised 11 November 2011; accepted 15 November 2011; published 20 January 2012.

[1] We estimate shear wave velocities in the shallow subsurface throughout Japan by applying seismic interferometry to the data recorded with KiK-net, a strong motion network in Japan. Each KiK-net station has two receivers; one receiver on the surface and the other in a borehole. By using seismic interferometry, we extract the shear wave that propagates between these two receivers. Applying this method to earthquake-recorded data at all KiK-net stations from 2000 to 2010 and measuring the arrival time of these shear waves, we analyze monthly and annual averages of the near-surface shear wave velocity all over Japan. Shear wave velocities estimated by seismic interferometry agree well with the velocities obtained from logging data. The estimated shear wave velocities of each year are stable. For the Niigata region, we observe a velocity reduction caused by major earthquakes. For stations on soft rock, the measured shear wave velocity varies with the seasons, and we show negative correlation between the shear wave velocities and precipitation. We also analyze shear wave splitting by rotating the horizontal components of the surface sensors and borehole sensors and measuring the dependence on the shear wave polarization. This allows us to estimate the polarization with the fast shear wave velocity throughout Japan. For the data recorded at the stations built on hard rock sites, the fast shear wave polarization directions correlate with the direction of the plate motion.

Citation: Nakata, N., and R. Snieder (2012), Estimating near-surface shear wave velocities in Japan by applying seismic interferometry to KiK-net data, *J. Geophys. Res.*, *117*, B01308, doi:10.1029/2011JB008595.

1. Introduction

[2] Seismic interferometry is a powerful tool to obtain the Green's function that describes wave propagation between two receivers [e.g., *Aki*, 1957; *Claerbout*, 1968; *Lobkis and Weaver*, 2001; *Roux and Fink*, 2003; *Schuster et al.*, 2004; *Wapenaar*, 2004; *Bakulin and Calvert*, 2006; *Snieder et al.*, 2006; *Wapenaar and Fokkema*, 2006]. Seismic interferometry is applied to ambient noise [e.g., *Hohl and Mateeva*, 2006; *Draganov et al.*, 2007, 2009; *Brenguier et al.*, 2008; *Stehly et al.*, 2008; *Lin et al.*, 2009], traffic noise [e.g., *Nakata et al.*, 2011], production noise [e.g., *Miyazawa et al.*, 2008; *Vasconcelos and Snieder*, 2008], earthquake data [e.g., *Larose et al.*, 2006, *Sens-Schönfelder and Wegler*, 2006; *Snieder and Şafak*, 2006; *Ma et al.*, 2008; *Ruigrok et al.*, 2010], and active sources [e.g., *Bakulin and Calvert*, 2004; *Mehta et al.*, 2008].

[3] In Japan, large seismometer networks, such as Hi-net, F-net, K-NET, and KiK-net [*Okada et al.*, 2004], are deployed. By using these networks for seismic interferometry, *Tonegawa et al.* [2009] extract the deep subsurface structure of the Philippine Sea slab. These data have also been used to observe time lapse changes in small regions [*Wegler and Sens-Schönfelder*, 2007; *Sawazaki et al.*, 2009; *Wegler et al.*, 2009; *Yamada et al.*, 2010]. Each KiK-net station has two receivers, one on the ground surface and the other at the bottom of a borehole. One can estimate the body wave velocity between two receivers by using seismic interferometry [*Trampert et al.*, 1993; *Snieder and Şafak*, 2006; *Mehta et al.*, 2007a; *Miyazawa et al.*, 2008].

[4] By applying seismic interferometry to KiK-net data, we analyze near-surface velocities throughout Japan. Because KiK-net has recorded strong motion seismograms continuously since the end of 1990s, the data are available for time lapse measurements. Measuring time lapse changes of the shallow subsurface is important for civil engineering and for estimating the site response to earthquakes. Previous studies extracted time lapse changes caused by earthquakes [*Li et al.*, 1998; *Vidale and Li*, 2003; *Schaff and Beroza*, 2004; *Wegler and Sens-Schönfelder*, 2007; *Brenguier et al.*, 2008]. Interferometry applied to a single KiK-net station has also been used to measure time lapse change due to earthquakes [*Sawazaki et al.*, 2009; *Yamada et al.*, 2010]. Interferometric studies have shown changes in the shear wave velocity caused by precipitation [*Sens-Schönfelder and Wegler*, 2006] and have measured shear wave splitting [*Bakulin and Mateeva*, 2008; *Miyazawa et al.*, 2008]. We study the annual and monthly averages of the shear wave velocity and the fast shear wave polarization directions for stations all over Japan, and the temporal change in shear

---

[1] Department of Urban Management, Kyoto University, Kyoto, Japan.

[2] Center for Wave Phenomena, Department of Geophysics, Colorado School of Mines, Golden, Colorado, USA.

0148-0227/12/2011JB008595

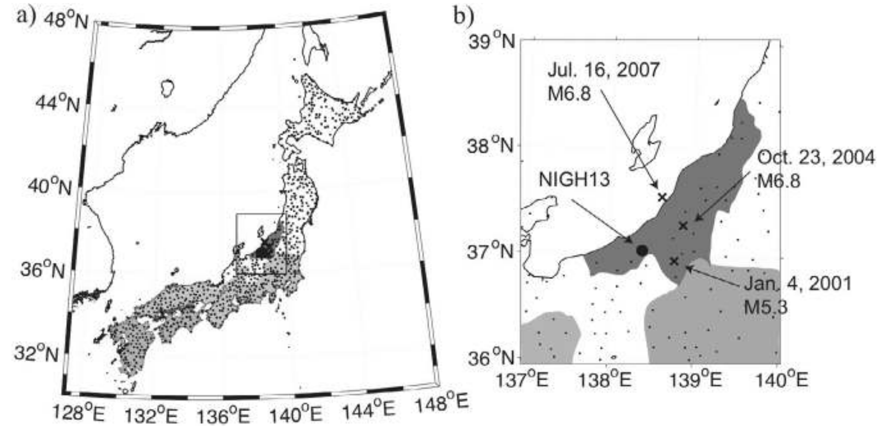

Figure 1. (a) KiK-net stations (December 2010). The black dots on the map represent the locations of the stations. The dark gray shows the area analyzed in section 6.1. The light gray illustrates the area where we apply the analysis for seasonal change (section 6.2). (b) Magnification of the rectangle area in Figure 1a. The large black circle indicates station *NIGH*13, which we use for examples of analysis in Figures 2, 4, 5, 6, 9, and 10. The black crosses depict the epicenters of three significant earthquakes that occurred in the vicinity.

wave velocity in the Niigata prefecture for three major earthquakes.

[5] This paper presents data processing of KiK-net data with seismic interferometry. We first introduce the properties of KiK-net. Next, we show the data analysis method. Then we present near-surface shear wave velocities in every part of Japan. Finally, we interpret these velocities to study time lapse changes, which are related to major earthquakes and precipitation, and present measurements of shear wave splitting.

2. KiK-net Data

[6] About 700 KiK-net stations are distributed in Japan (Figure 1). The stations are operated by the National Research Institute for Earth Science and Disaster Prevention (NIED). Each station has a borehole and two seismographs which record strong motion at the bottom and top of the borehole. Each seismograph has three components: one vertical component and two horizontal components. Although the two horizontal components of the surface seismograph are oriented in the north-south and east-west directions, respectively, the horizontal components of the borehole seismograph are not always aligned with the north-south and east-west directions because of technical limitations. Therefore, we rotate the directions of the borehole seismograph north-south and east-west directions before data processing. The depth of about 25% of the boreholes is 100 m, and the other boreholes are at greater depth. Since our target is the near surface, we use the stations with a depth less than 525 m, which accounts for 94% of the stations. The sampling interval is either 0.005 or 0.01 s, depending on the station and the recording date.

[7] We show example records of an earthquake in Figure 2. Figure 2a illustrates bandpass-filtered time series, and Figure 2b illustrates the power spectra of the unfiltered data. As shown in Figure 2b, most energy is confined to 1–13 Hz, and we apply a bandpass filter over this frequency range for all data processing. In Figure 2, UD denotes the vertical component, NS denotes the north-south direction horizontal component, and EW denotes the east-west direction horizontal component. In Figure 2a, the P wave arrives at around 7 s, and the shear wave arrives at around 14 s.

[8] All the used events are at a depth greater than 10 km. Because of this large depth compared to the depth of the boreholes and the low velocity in the near surface, the waves that travel between the sensors at each station propagate in the near-vertical direction as plane waves. We compute the angle of the incoming wave at the borehole receiver by using one-dimensional ray tracing to confirm that the wave propagating between the borehole and surface seismometers, propagates in the near-vertical direction. We use the velocity model of *Nakajima et al.* [2001] to determine the ray parameter p of the ray between each earthquake and the borehole sensor. The angle of incidence θ of the wave propagating from the borehole receiver to the surface receiver is given by $\cos\theta = \sqrt{1 - p^2 v^2}$, where v is the average shear wave velocity between these sensors as determined in this study. A bias in the velocity estimation due to nonvertical propagation depends on the deviation of $\cos\theta$ from its value for vertical incidence, $\cos 0° = 1$.

3. Retrieval of the Wavefield Between Receivers

[9] We apply seismic interferometry to the recorded earthquake data of each station for retrieving the wavefield where the borehole receiver behaves as a virtual source. Several algorithms have been used in seismic interferometry to obtain the wavefield. These include cross correlation [e.g., *Claerbout*, 1968; *Bakulin and Calvert*, 2004], deconvolution [e.g., *Trampert et al.*, 1993; *Snieder and Şafak*, 2006], cross coherence [e.g., *Aki*, 1957; *Prieto et al.*, 2009], and multidimensional deconvolution [e.g., *Wapenaar et al.*, 2008; *Minato et al.*, 2011].

[10] We introduce the cross-correlation and deconvolution algorithms. We denote the wavefield, excited at source location $\mathbf{s}$ that strikes the borehole receiver at location $\mathbf{r_b}$ by $u(\mathbf{r_b}, \mathbf{s}, \omega) = S(\mathbf{r_b}, \mathbf{s}, \omega)$, where $S(\mathbf{r_b}, \mathbf{s}, \omega)$ is the incoming

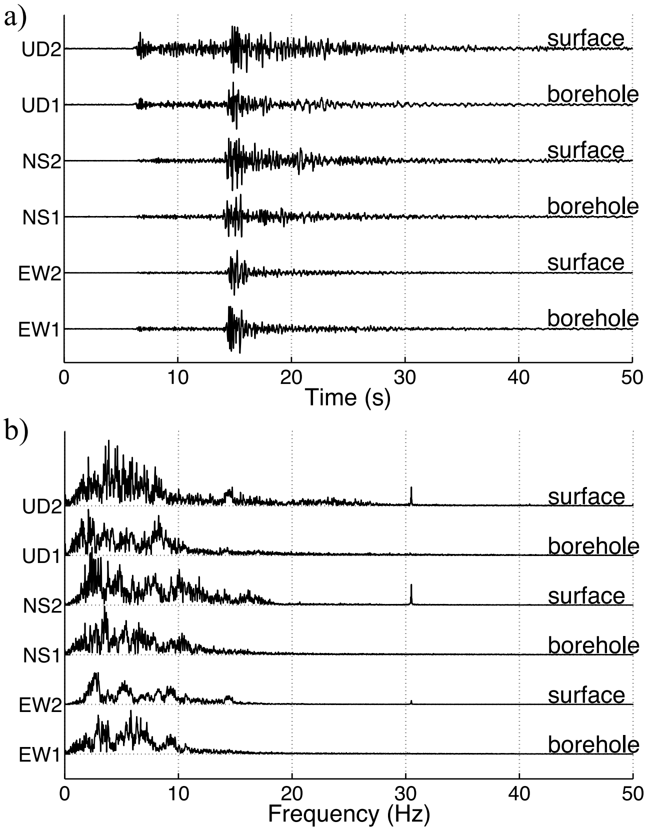

Figure 2. An earthquake recorded at all channels of station *NIGH*13 (latitude 37.0514°N and longitude 138.3997°E). This earthquake occurred at 14:59:19.56, 27 October 2004. The epicenter is at latitude 37.2204°N and longitude 138.5608°E and the depth is 11.13 km. The magnitude of this earthquake is $M_{JMA}4.2$. UD represents the vertical component, NS represents the north-south direction horizontal component, EW represents the east-west direction horizontal component, 1 represents the borehole seismograph, and 2 represents the surface seismograph. (a) The bandpass-filtered (1–13 Hz) time series. (b) The power spectra of the unfiltered records.

wavefield that includes the source signature of the earthquake and the effect of propagation such as attenuation and scattering, in the frequency domain. The corresponding wavefield recorded at the surface receiver at location $\mathbf{r}_s$ is given by

$$u(\mathbf{r}_s, \mathbf{s}, \omega) = 2G(\mathbf{r}_s, \mathbf{r}_b, \omega) S(\mathbf{r}_b, \mathbf{s}, \omega), \tag{1}$$

where the factor 2 is due to the presence of the free surface at $\mathbf{r}_s$. Because the wavefield striking the borehole receiver is close to a vertically propagating plane wave, $G(\mathbf{r}_s, \mathbf{r}_b, \omega)$ is the plane wave Green's function that accounts for the propagation from the borehole seismometer to the surface seismometer.

[11] The cross-correlation approach to retrieve the wavefield in one dimension is given by *Wapenaar et al.* [2010]:

$$|S(\mathbf{r}_b, \mathbf{s}, \omega)|^2 G(\mathbf{r}_s, \mathbf{r}_b, \omega) = \frac{2j\omega}{\rho c} u(\mathbf{r}_s, \mathbf{s}, \omega) u^*(\mathbf{r}_b, \mathbf{s}, \omega), \tag{2}$$

where ρ is the mass density of the medium, c the wave propagation velocity, j the imaginary unit, and $*$ the complex conjugate. The regularized deconvolution, which is similar to cross correlation, is given by

$$G(\mathbf{r}_s, \mathbf{r}_b, \omega) = \frac{u(\mathbf{r}_s, \mathbf{s}, \omega)}{u(\mathbf{r}_b, \mathbf{s}, \omega)} \approx \frac{u(\mathbf{r}_s, \mathbf{s}, \omega) u^*(\mathbf{r}_b, \mathbf{s}, \omega)}{|u(\mathbf{r}_b, \mathbf{s}, \omega)|^2 + \epsilon}, \tag{3}$$

where ϵ is a regularization parameter [*Mehta et al.*, 2007a, 2007b]. The deconvolution is potentially unstable due to the spectral devision, and we avoid divergence by adding a positive constant ϵ to the denominator (equation (3)). Note that the deconvolution eliminates the imprint of waveform $S(\mathbf{r}_b, \mathbf{s}, \omega)$, which is incident on the borehole receiver. We derive the features of cross-correlation and deconvolution interferometry in Appendix A.

4. Data Processing

[12] We use 111,934 earthquake-station pairs that are recorded between 2000 and 2010. The magnitude range is confined between 1.9 and 8.2. The cosine of the angle of incidence $\cos\theta$ of the wave propagating between the receivers at each station is greater than 0.975, even for the events that are the furthest away. The bias introduced by nonvertical propagation thus is less than 2.5%, and for most measurements it is much smaller. First, we check the data quality and drop some seismograms by a visual inspection using the signal-to-noise ratio as a criterion. Additionally, we discard stations with a borehole seismometer at a depth greater than 525 m because we focus this study on the near surface. We remove the DC component of the data by subtracting the average of each seismogram. For aligning the directions of the borehole receiver to the exact north-south and east-west directions, we rotate the borehole receiver using the rotation angle provided by NIED [*Shiomi et al.*, 2003]. Because the sampling interval is not small compared to the travel time of P waves between the borehole and surface seismometers, we focus on the shear wave and only analyze the horizontal components.

[13] We first apply deconvolution interferometry to the motion in the north-south direction of each surface-borehole pair. In this study, for reasons explained below, deconvolution interferometry gives more consistent estimates of the Green's function than does cross-correlation interferometry. We choose ϵ in equation (3) to be 1% of the average power spectrum of the borehole receiver in the frequency range 1–13 Hz because we find empirically that this is the smallest regularization parameter to obtain stable wavefields. We apply a band-pass filter from 1–13 Hz after applying deconvolution interferometry.

[14] In this paper, we average in three ways to interpret the wavefields. The first method is the *annual stack*, where we average the deconvolved waveforms over the earthquakes recorded in each year. In the second averaging method, we average the deconvolved waves over all earthquakes recorded in each month over the 11 years (January 2000–2010, February 2000–2010, .., and December 2000–2010). We call this average the *monthly stack*. In the third method, which

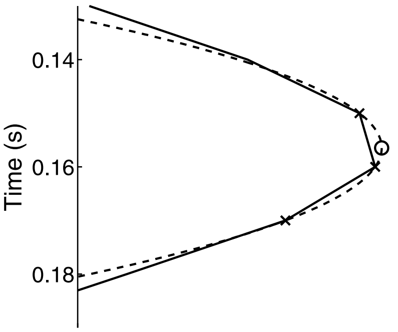

Figure 3. Quadratic interpolation. Using the three largest amplitude points (crosses), we interpolate the highest amplitude point (circle) by estimating the quadratic curve through the three highest amplitude points.

we use for analyzing the influence of major earthquakes, we average over three months after a significant earthquake.

4.1. Estimating the Shear Wave Velocity

[15] Before we apply annual stacking or monthly stacking, we resample the data from 0.005 s interval to 0.01 s interval if the data that are stacked include both 0.005 s and 0.01 s sampling interval data. After stacking, we estimate the arrival time by seeking the three adjacent samples with the largest values and apply quadratic interpolation to find the time at which the deconvolved data have a maximum amplitude (Figure 3). This time is the travel time for a shear wave that propagates between the borehole and surface sensors. We use this travel time to compute the shear wave velocity of the region between the two receivers.

4.2. Computing the Average and Standard Deviation of the Velocity of the Annual or Monthly Stacks

[16] To interpret time lapse variations in the velocities, we need to compute the average and standard deviation of the velocities within a region. Let us denote the estimated velocity by $v_i(m, y)$, where v_i is the shear wave velocity at station i, in month m, and year y. This velocity is already averaged over each month. Each station has a different velocity. In order to quantify the time lapse variations of the velocity, we subtract the average value of each station before calculating temporal variation in the annual or monthly average:

$$\Delta v_i(m,y) = v_i(m,y) - \bar{v}_i, \tag{4}$$

where $\bar{v}_i$ is an average velocity of station i over all months and years. Then we compute either the annual or monthly average of the velocity variation over stations Δv, and we also compute the standard deviation of this quantity.

4.3. Comparison Between Cross-Correlation and Deconvolution Interferometry

[17] We compare the cross-correlation and deconvolution approaches using the annual stacked wavefields (Figure 4). We show the locations of the epicenters of the used earthquakes in Figure 5. The annual stacks of the waveforms obtained by cross correlation are shown in Figure 4a. These waveforms are not repeatable from year to year and often do not show a pronounced peak at the arrival time of the shear wave at around $t = 0.15$ s. We attribute the variability in these waveforms to variations in the power spectrum $|S(\boldsymbol{r_b}, \boldsymbol{s}, \omega)|^2$ of the waves incident at the borehole receiver (equation (A1)). In contrast, the annual stacks of the waveforms obtained by deconvolution shown in Figure 4b are highly repeatable and show a consistent peak at the arrival time of the shear wave. The consistency of these waveforms is due to the deconvolution that eliminates the imprint of the incident wave $S(\boldsymbol{r_b}, \boldsymbol{s}, \omega)$ (equation (A2)). Consistent with earlier studies [*Trampert et al.*, 1993; *Snieder and Şafak*, 2006], we use deconvolution to extract the waves that propagate between the seismometers at each KiK-net station.

4.4. Shear Wave Splitting

[18] We investigate shear wave splitting by measuring the shear wave velocity as a function of the polarization. We rotate both surface and borehole receivers from 0° to 350° using a 10° interval. The north-south direction is denoted by 0°, and the east-west direction by 90°. Because a rotation over 180° does not change the polarization, the 0° to 170° wavefields are the same as the 180° to 350° data. We apply deconvolution interferometry to the rotated wavefields,

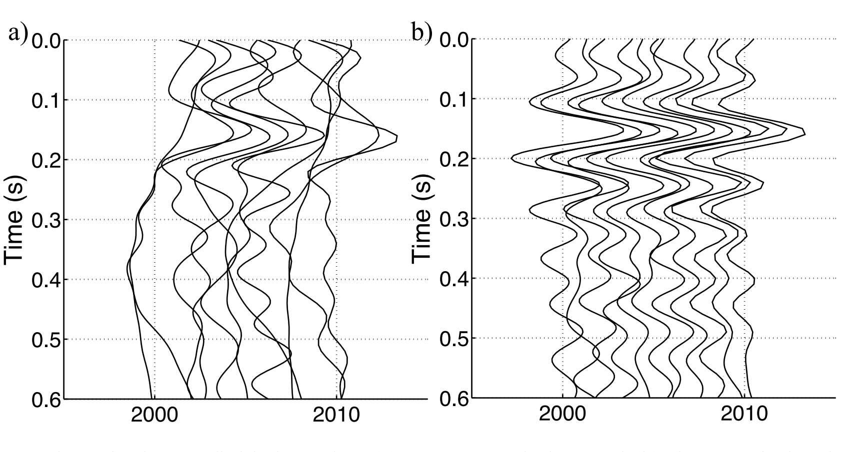

Figure 4. Annual stacked wavefields by using (a) cross correlation and (b) deconvolution interferometry at station *NIGH*13. The surface and borehole receiver orientation directions are north-south. Epicenter locations are illustrated in Figure 5.

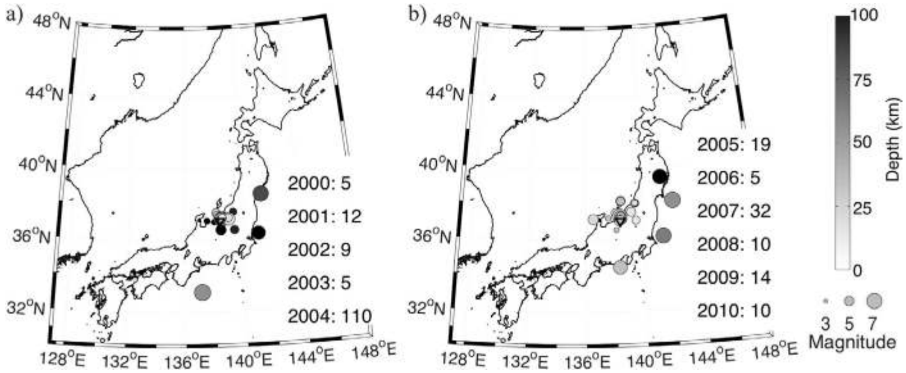

Figure 5. Epicenters used in Figure 4 (a) from 2000 to 2004 and (b) from 2005 to 2010 at station *NIGH*13. At the right in each panel, we show the number of earthquakes we use to obtain the waveforms in Figure 4 in each year. The size of each circle refers the magnitude of each earthquake and the color indicates the depth. The white triangle illustrates the location of station *NIGH*13. Because of the proximity of events, many circles overlap.

located at the surface and borehole receivers with the same polarizations, for determining the velocity of each polarization. Because the velocity for each polarization is related to the velocities of the fastest and slowest shear waves (Appendix B), we can estimate shear wave splitting from the velocity difference. We cross correlate the deconvolved wavefield for every used polarization (from 0° to 350° in 10° intervals) with the deconvolved wavefield obtained from the motion in the north-south direction. This allows us to quantify the polarization dependence of the shear wave velocity. Similar to the process described in section 4.1, we compute annual stacks of cross-correlated wavefields and pick the peak amplitudes of stacked wavefields by using quadratic interpolation.

[19] We can separate the velocity $v(\phi)$ as a function of polarization direction ϕ into the isotropic and anisotropic terms using a Fourier series expansion (Appendix C):

$$v(\phi) = v_0 + v_1 \cos 2\phi + v_2 \sin 2\phi. \tag{5}$$

In this expression, v_0 is the isotropic component of the velocity, and $\sqrt{v_1^2 + v_2^2}$ the anisotropy. We assume the splitting time to be much smaller than the period of the wavefield. Because the wavefields of each polarization data are symmetric by 180°, the anisotropy depends on polarization through a dependence of 2ϕ.

5. Retrieved Near-Surface Shear Wave Velocities in Japan

[20] Using deconvolution interferometry at each station, we obtain the wavefield that corresponds to a plane wave propagating in the near-vertical direction ($\cos\theta > 0.975$) between the borehole receiver and surface receiver at each station. In this section, we show the wavefields of the annual stack, monthly stack, and shear wave splitting.

5.1. Annual and Monthly Stacks

[21] Figure 6 shows the annual stacked wavefields at station *NIGH*13 represented by the large black circle in Figure 1. At this station, the sampling interval is 0.005 s until 2007 and is 0.01 s after 2008. In Figure 6, the deconvolved wavefields have good repeatability and a pronounced peak amplitude. After we apply quadratic interpolation (section 4.1), the determined arrival times (the black circles in Figure 6) correlate well with the travel time which is obtained from logging data (the horizontal line in Figure 6). The logging data is measured using a logging tool and by Vertical Seismic Profiling (VSP). The seismic source of VSP is a vertical component vibrator. For finite offsets this source generates shear waves. We determine the average velocity from the logging data by computing the depth average of the slowness, because this quantity accounts for the vertical travel time. Because of the quadratic interpolation, the measured travel times show variations smaller than the original sampling time.

[22] After determining the arrival times of all stations, we compute the shear wave velocities by using the known depth of the boreholes. Applying triangle-based cubic

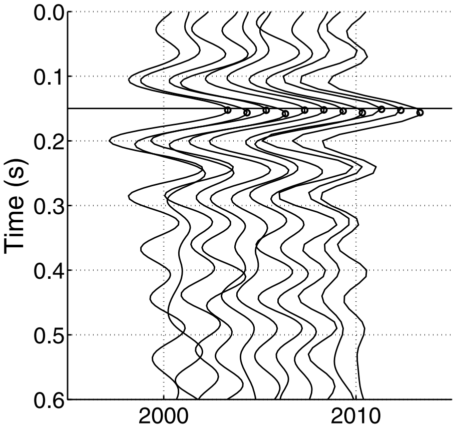

Figure 6. Annual stacked wavefields (curves) with the interpolated largest amplitude (circles) at station *NIGH*13. The horizontal line at around 0.15 s is the shear wave arrival time determined from logging data. From left to right, we show annual stacks from 2000 to 2010. The source and receiver polarization directions are the north-south direction.

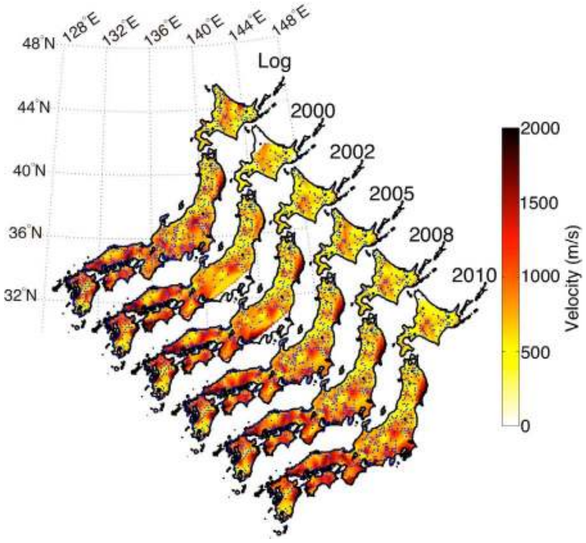

Figure 7. Shear wave velocities obtained from logging data (Log) and estimated by annual stacked seismic interferometry using earthquake data at the north-south polarization (excerpted 2000, 2002, 2005, 2008, and 2010). The blue dots on a map represent the station locations which we use to make the map. We interpolate velocities between stations by triangle-based cubic interpolation [*Lawson*, 1984]. The longitude and latitude belong to the map in the upper left. The number of right upper side of each map shows the year of data.

interpolation [*Lawson*, 1984] between stations, we create the shear wave velocity map of Japan in each year (Figure 7). To reduce the uncertainty of the velocity estimation we use only the stations which give deconvolved waves with an arrival time greater than 0.1 s. Thus, we obtain the near-surface shear wave velocities throughout Japan by applying seismic interferometry to KiK-net data. The shear wave velocity obtained from logging data is shown in the top left in Figure 7. Note that the velocities measured in different years are similar. In Figure 8, we crossplot the velocities estimated by interferometry in 2008 and obtained from logging data. The data are concentrated along the black line, which indicates the degree of correlation between the shear wave velocity obtained from logging data and from seismic interferometry.

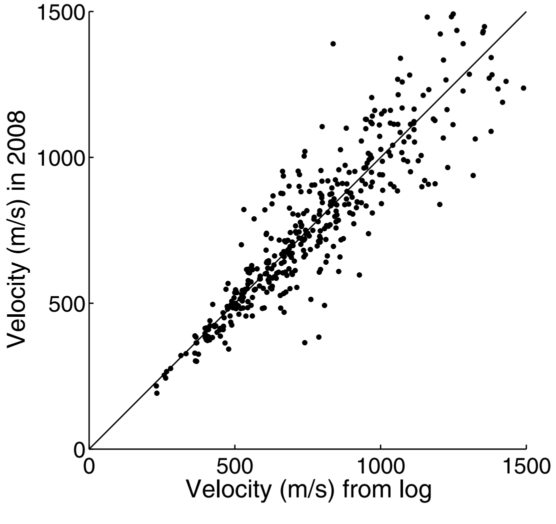

Figure 8. Crossplot of velocities computed from logging data and by seismic interferometry in 2008. The black line indicates equal velocities.

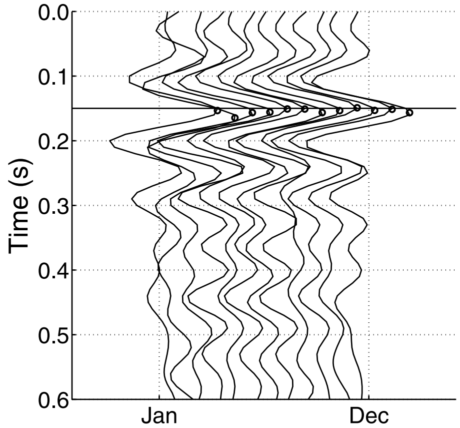

Figure 9. Monthly stacked wavefields (curves) with the interpolated largest amplitude (circles) at station *NIGH*13. The horizontal line at around 0.15 s is the shear wave arrival time obtained from logging data. From left to right, we depict monthly stacks from January to December. Each trace is stacked over the 11 years (January 2000–2010, February 2000–2010, .., and December 2000–2010). The source and receiver polarization directions are the north-south direction.

[23] We also analyze seasonal changes and show the monthly stacked wavefields at station *NIGH*13 in Figure 9. The monthly stacked wavefields also have good repeatability between different months.

5.2. Shear Wave Splitting

[24] In Figure 10a, we show the wavefields of the shear wave splitting analysis at station *NIGH*13 in 2010 that are obtained by the sequence of deconvolution and cross correlation described in section 4.4. Each trace is plotted at the angle that is equal to the shear wave polarization used to compute that trace. The thick solid line in Figure 10a shows the interpolated maximum amplitude time of each waveform. The dashed circle shows the arrival time for the wave polarized in the north-south direction. For the polarizations where the thick solid line is outside of the dashed circle, the shear wave velocity is slower. The fast and slow shear polarization directions in Figure 10a are 22° and −71° clockwise from the north-south direction, respectively. The angle between these fast and slow directions is 93°, which is close to 90° as predicted by theory [*Crampin*, 1985] (see also Appendix C). The 3° discrepancy could be caused by data noise or discretization errors. At station *NIGH*13 in 2010, the fast polarization shear wave velocity v_{fast} is 638 m/s, the slow velocity v_{slow} is 593 m/s, and the anisotropy parameter $(v_{fast} - v_{slow})/v_{fast}$ is 7% (see Figure 10b). The difference of the arrival times between the fast and slow polarization velocity wavefields is much smaller than the

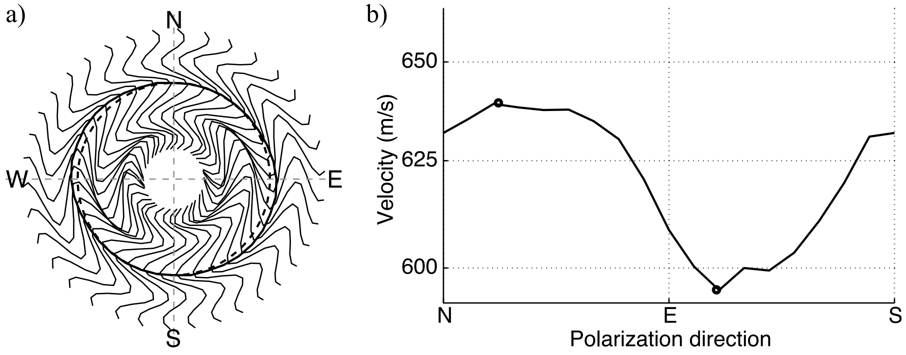

Figure 10. (a) Cross correlograms along every 10° polarization direction in 2010 at station *NIGH*13. Each trace is plotted at an angle equal to the polarization direction used to construct that trace. The dashed circle indicates the peak amplitude time of the north-south direction, and the thick solid line represents the peak amplitude time for each polarization direction. (b) Shear wave velocities computed from the thick solid line in Figure 10a. Black circles represent the quadratic interpolated fast and slow polarization shear wave velocities.

period of a wavefield when the borehole depth is less than 525 m.

6. Interpretation of Shear Wave Velocities and Shear Wave Splitting

6.1. Influence of Major Earthquakes

[25] The near-surface shear wave velocity in Japan is similar between years (see Figure 7), which means the near-surface structure is basically stable. In this section, we focus on a small region. We use Δv (calculated by the method presented in section 4.2) and the fast shear wave polarizations shown in Figure 11 to analyze the influence of major earthquakes in the Niigata prefecture (the dark shaded area in Figure 1). Three significant earthquakes, shown by the dashed arrows in each panel, occurred during the 11 years.

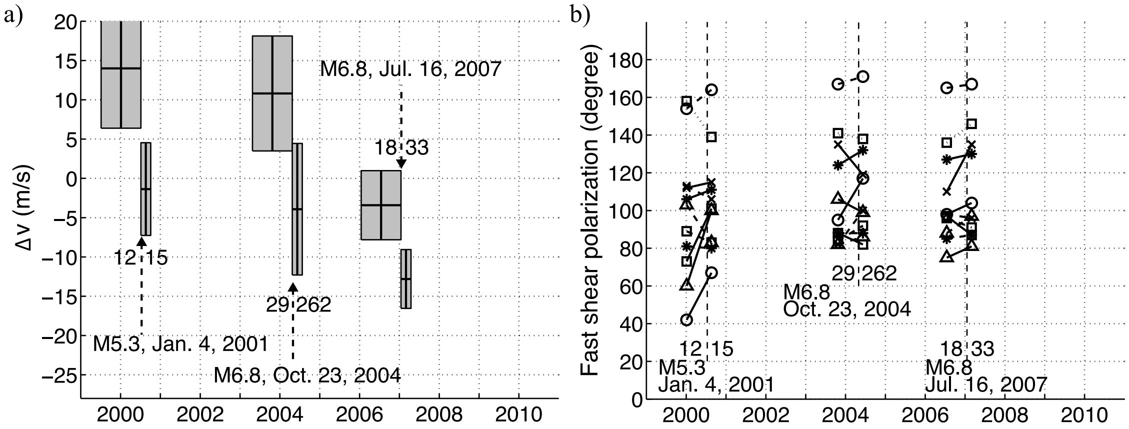

Figure 11. (a) The isotropic component of the shear wave velocity (Fourier coefficient v_0) averaged over one year before and three months after three major earthquakes. (b) The direction of the fast shear wave polarization averaged over same intervals. All data are computed for stations in the Niigata prefecture (the dark shaded area in Figure 1). In each image, the label of the year is placed in the middle of each year. The dashed arrows in Figure 11a and the vertical dashed lines in Figure 11b indicate the times of the three major earthquakes shown with the black crosses in Figure 1. The numbers at the left and right of dashed arrows (Figure 11a) and lines (Figure 11b) are the number of earthquakes we use for determining velocities and polarizations before and after the major earthquakes, respectively. In Figure 11a, each velocity is the velocity variation Δv in equation (4). The horizontal extent of each box depicts the time interval used for averaging (one year before and three months after the major earthquakes). The vertical extent of each box represents the standard deviation of the velocity in the area computed by the method in section 4.2. The horizontal line in each box indicates average velocity Δv in each time interval, and the vertical line the center of each time interval. In Figure 11b, we use only the stations with significant anisotropy ($(v_{fast} - v_{slow})/v_{fast} \geq 1\%$). We select 11 stations from 19 stations and depict the fast shear wave polarization directions with different symbols or lines. Each symbol is placed at the center of each time period.

[26] Figure 11a shows the velocity variation Δv for the isotropic component v_0 computed by equation (5) compiled over periods one year before and three months after the major earthquakes. We use all stations in the Niigata prefecture and compute the average over the stations. Each box depicts the time range (horizontal extent) and the error in the average velocity over that time interval (vertical length). The error in the velocity is given by the standard deviation of measurements from different earthquakes in each time interval (section 4.2). In Figure 11a, these average velocities show significant velocity reduction after the major earthquakes. The average isotropic velocity of all stations in the region from 2000 to 2010 is 662 m/s, and the relative velocity change of each earthquake is around 3–4%. Similar velocity variations caused by major earthquakes were reported earlier; for example, *Sawazaki et al.* [2009] analyze the variations caused by the 2000 Western-Tottori Earthquake, *Yamada et al.* [2010] analyze the variations caused by the 2008 Iwate-Miyagi Nairiku earthquake using KiK-net stations, while *Nakata and Snieder* [2011] observe a velocity reduction of about 5% after the 2011 Tohoku-Oki earthquake. To increase the temporal resolution of the velocity change, we compute velocity changes averaged over periods one year before and three months after the major earthquakes (Figure 11a) because *Sawazaki et al.* [2009] found that the velocity reduction is sustained over a period of at least three months after an earthquake.

[27] The stations on soft rock sites have a greater velocity reduction than those on hard rock sites. (We define soft and hard rock sites from the estimated shear wave velocity; hard rock sites have a shear wave velocity greater than 600 m/s, while soft rock sites have a shear wave velocity less than 600 m/s.) For the used event-station pairs, the velocity reduction does not change measurably with the distance from the epicenter. This is an indication that the velocity reduction depends mostly on the local geology. The velocity reduction can be due either to the opening and closing of existing fractures, to the creation of new fractures, or to the change in the shear modulus caused by changes in the pore fluid pressure because of shaking-induced compaction [*Das*, 1993, Figure 4.24].

[28] The relative velocity reduction is smaller than the reduction found by *Wu et al.* [2009] because of the averaging over stations and over earthquakes recorded over a period of three months. *Wu et al.* [2009] use a single station located on a soft rock site and do not average over several months. *Wegler et al.* [2009] estimate the velocity reduction in deeper parts of the subsurface, and the velocity reduction they find is small (0.3–0.5 %). From this we infer that the velocity reduction due to a major earthquake is most pronounced in near surface, especially for soft rock sites.

[29] We also obtain the polarization directions of the fast shear waves before and after the major earthquakes by averaging over the same time intervals as used in Figure 11a (Figure 11b). The direction of the fast shear wave polarization does not show a significant change after the earthquakes, hence it seems to be unaffected by these earthquakes. The average standard deviation of the polarization direction of all stations in the Niigata prefecture between 2000 and 2010 is 15°, which represents the accuracy of the fast shear wave velocity polarization direction.

6.2. Influence of Precipitation

[30] We compute the monthly averaged shear wave velocities of the north-south polarization (Figure 12a) to investigate a possible seasonal velocity variation related to precipitation. We use only the data in southern Japan (the light shaded area in Figure 1) because that region has a more pronounced seasonal precipitation cycle than northern Japan. Figure 12a illustrates a significant velocity difference between spring/summer and fall/winter. We calculate the average velocities over the stations with the 15% slowest shear wave velocities in the area because these stations are located at soft rock sites and are therefore influenced more by precipitation than the station at hard rock sites. We compare the monthly averaged velocities with the monthly average of precipitation (observed by the Japan Meteorological Agency (JMA)) computed from precipitation records over 30 years (Figure 12b). Note the negative correlation between the shear wave velocity and precipitation (i.e., when it rains, the velocity decreases), which is consistent with the findings of *Sens-Schönfelder and Wegler* [2006].

[31] For comparison, for the stations with the 85% fastest shear wave velocities in the area (Figure 12c) the shear wave velocity does not vary with precipitation. The cause of the velocity reduction is the decreased effective stress of the soil due to the infiltration of water that increases the pore pressure [*Das*, 1993, section 4.19; *Chapman and Godin*, 2001; *Snieder and van den Beukel*, 2004]. We assume that for soft rock sites most of the velocity change is caused by the effective stress change because *Snieder and van den Beukel* [2004] show that the relative density change with pore pressure is much smaller than the relative change in the shear modulus.

6.3. Shear Wave Splitting and the Direction of the Plate Motion

[32] Using shear wave splitting analysis, we determine fast shear wave polarization directions of every station (illustrated by the black arrows in Figure 13a). These directions are averaged over all years from 2000 to 2010 because the temporal changes in the direction are small (see Figure 11b). We plot the directions of all stations which have an anisotropy parameter $(v_{fast} - v_{slow})/v_{fast} \geq 1\%$ because the uncertainty in the direction of the fast shear polarization is large when the anisotropy is small. In Figure 13a, we also plot the direction of the plate motion at each station (the gray arrows), estimated from GPS data [*Sagiya et al.*, 2000]. Each arrow is normalized to the same length.

[33] In Figure 13b, we plot only the stations which have an anisotropy parameter larger than 1% and a north-south polarization shear wave velocity faster than 600 m/s; these stations are located on hard rock sites. The average absolute angle between the directions of fast shear polarization and the plate motion in these stations is 16°, and this average angle of the stations which have a shear wave velocity less than 600 m/s is 36°. Therefore, the fast shear wave polarization on hard rock sites correlates more strongly with the direction of the plate motion than the polarization on soft rock sites. The 16° angle is close to the 15° standard deviation angle of each station computed in section 6.1. The near-surface polarization in the western part of Figure 13b correlates well with observations of the shear

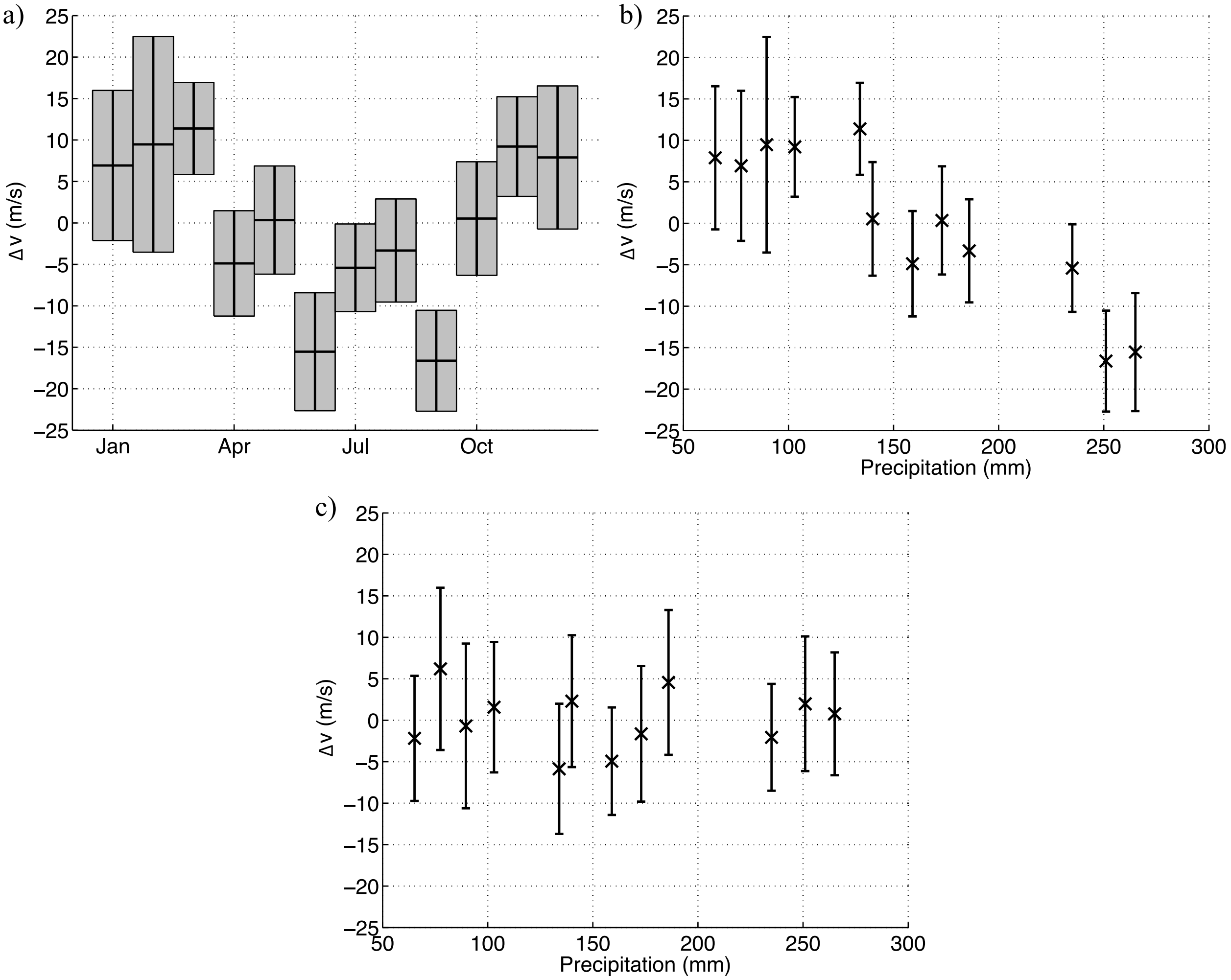

Figure 12. Seasonal dependence of shear wave velocity. (a) Variation of the average monthly velocities stacked over the period 2000 through 2010 in southern Japan (the light gray area in Figure 1). We use the stations with the 15% slowest velocities in the area. The horizontal extent of each box shows time interval used for averaging, and the vertical extent the standard deviations of all receivers in the time interval computed by the method in section 4.2. The horizontal line in each box indicates average velocity Δv in each time interval, and the vertical line the center of each time interval. (b) Crossplot between monthly precipitation (provided by JMA) and the average velocity Δv with error bars. (c) Crossplot between monthly precipitation and the average velocity Δv with error bars using the stations with the 85% fastest velocities in the area.

wave polarization at greater depth [*Okada et al.*, 1995; *Nakajima and Hasegawa*, 2004; *Nakajima et al.*, 2006], but this agreement does not hold in the regions further east.

[34] We present a crossplot of the directions of the fast shear wave polarization and the plate motion for stations all over Japan (Figure 14), where we only used the stations which have an anisotropy parameter greater than 1% and a shear wave velocity faster than 600 m/s. The red area in Figure 14 indicates that for most stations the direction of the plate motion is between 90° and 140°, and that this direction correlates with the polarization direction of the fast shear wave. The near-surface stress directions on hard rock sites is presumably related to the plate motion because the stress field related to the plate motion changes the properties of fractures. Note that the used shear waves sample the shallow subsurface (down to about several hundreds of meters). It is remarkable that the shear wave velocities in the near surface at hard rock sites correlate with tectonic process (plate motion) that extends several tens of kilometers into the subsurface.

7. Conclusion

[35] We obtain annual and monthly averaged near-surface shear wave velocities throughout Japan by applying seismic interferometry to KiK-net data. Deconvolution interferometry yields more repeatable and higher resolution wavefields than does cross-correlation interferometry. Because picked arrival times in waveforms are generally stable over time and consistent with logging data, the near-surface has a stable shear wave velocity. After three strong earthquakes in the Niigata prefecture, however, the shear wave velocity is

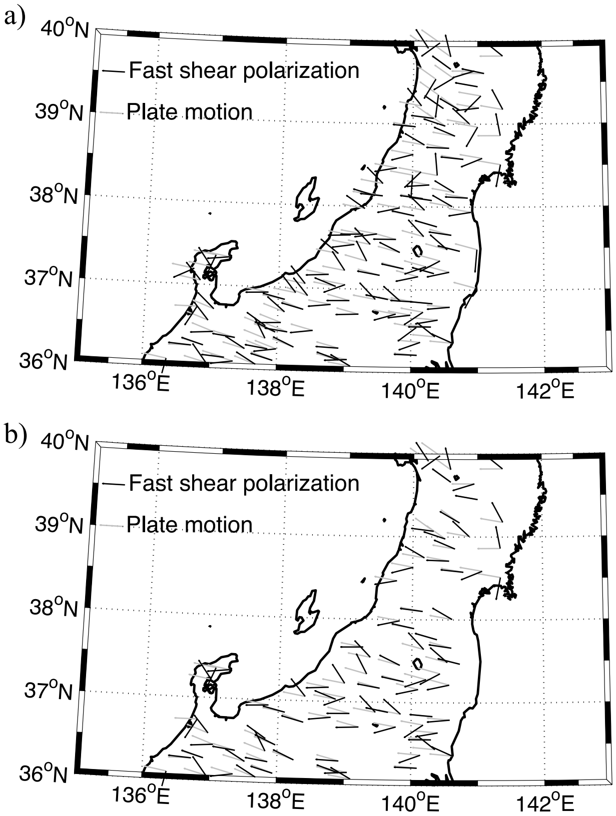

Figure 13. (a) Fast shear wave polarization directions (black lines) and the direction of the plate motion (gray lines) estimated from GPS data [*Sagiya et al.*, 2000] at the stations with significant anisotropy ($(v_{fast} - v_{slow})/v_{fast} \geq 1\%$). (b) Extracted stations from Figure 13a with shear wave velocity faster than 600 m/s.

reduced. By computing the monthly stacked velocity, we observe a velocity variation on stations placed on soft rock that has a negative correlation with precipitation. We also observe shear wave splitting. The fast shear wave polarization direction on a hard rock site correlates with the direction of the plate motion. Because the shear wave velocity is related to ground soil strength, these velocities are useful for civil engineering, site characterization, and disaster prevention.

Appendix A: 1-D Seismic Interferometry

[36] We explain in this appendix why deconvolution interferometry is suitable for this study. Figure A1 illustrates the model of interferometry using a KiK-net station and an earthquake. The incoming wavefield $S(\mathbf{r_b}, \mathbf{s}, \omega)$, propagating from source $\mathbf{s}$ to receiver $\mathbf{r_b}$, is given by $G(\mathbf{r_b}, \mathbf{s}, \omega)W(\mathbf{s}, \omega)$, where G is the Green's function including any unknown complex effect of wave propagation such as scattering and attenuation, and W the source signature in the frequency domain. Assuming that the subsurface is homogeneous between the receivers, the received wavefield at surface receiver $\mathbf{r_s}$ is $2S(\mathbf{r_b}, \mathbf{s}, \omega)e^{jkz_b}e^{-\gamma z_b}$, where γ is the attenuation coefficient and k the wave number. Because of the free surface, the amplitude of the wavefield at the surface is multiplied by a factor 2. We assume that there are no multiples between the two receivers. The reflected wavefield from the surface at the borehole receiver $\mathbf{r_b}$ is $S(\mathbf{r_b}, \mathbf{s}, \omega) e^{2jkz_b}e^{-2\gamma z_b}$, and the total wavefield at $\mathbf{r_b}$ is $S(\mathbf{r_b}, \mathbf{s}, \omega) + S(\mathbf{r_b}, \mathbf{s}, \omega)e^{2jkz_b}e^{-2\gamma z_b}$. Applying cross-correlation interferometry to these wavefields yields

$$\begin{aligned} u(\mathbf{r_s},\mathbf{s},\omega)u^*(\mathbf{r_b},\mathbf{s},\omega) &= 2S(\mathbf{r_b},\mathbf{s},\omega)e^{jkz_b}e^{-\gamma z_b} \\ &\qquad \left[S^*(\mathbf{r_b},\mathbf{s},\omega)+S^*(\mathbf{r_b},\mathbf{s},\omega)e^{-2jkz_b}e^{-2\gamma z_b}\right] \\ &\approx 2|S(\mathbf{r_b},\mathbf{s},\omega)|^2 e^{jkz_b}e^{-\gamma z_b} \end{aligned} \tag{A1}$$

when we consider only the first arrival. Using deconvolution interferometry, we obtain

$$\begin{aligned} \frac{u(\mathbf{r_s},\mathbf{s},\omega)}{u(\mathbf{r_b},\mathbf{s},\omega)} &= \frac{2S(\mathbf{r_b},\mathbf{s},\omega)e^{jkz_b}e^{-\gamma z_b}}{S(\mathbf{r_b},\mathbf{s},\omega)+S(\mathbf{r_b},\mathbf{s},\omega)e^{2jkz_b}e^{-2\gamma z_b}} \\ &\approx 2e^{jkz_b}e^{-\gamma z_b}, \end{aligned} \tag{A2}$$

where we also only retain the first arrival. The plane wave Green's function excited at $\mathbf{r_b}$ and received at $\mathbf{r_s}$ is equal to $2e^{jkz_b}e^{-\gamma z_b}$ in the frequency domain. Let us compare equations (A1), (A2), and the Green's function. The wavefield retrieved by cross-correlation interferometry is complicated because equation (A1) includes the power spectrum $|S(\mathbf{r_b}, \mathbf{s}, \omega)|^2$. This term is different for different earthquakes. In contrast, deconvolution interferometry eliminates the incoming wave $S(\mathbf{r_b}, \mathbf{s}, \omega)$, and thus provides a more accurate estimate of the Green's function. When we stack deconvolved wavefields over earthquakes, the accuracy of this estimate is improved. Because the deconvolved waves do not depend on the power spectrum of the incident wave $|S(\mathbf{r_b}, \mathbf{s}, \omega)|^2$, the deconvolved wavefields are more reproducible than those obtained from cross correlation.

Appendix B: Shear Wave Splitting

[37] Usually, shear wave splitting is analyzed with Alford rotation [*Alford*, 1986; *Thomsen*, 1988]. This procedure is

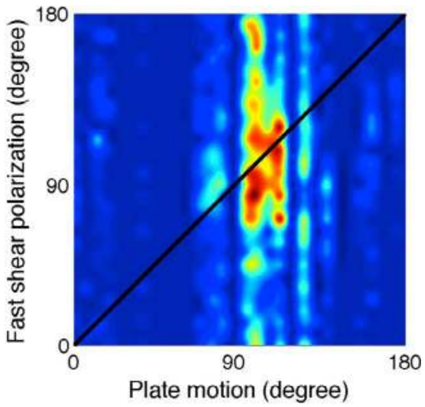

Figure 14. Crossplot between the direction of the plate motion and the fast shear wave polarization directions. We use the stations which have faster than 600 m/s shear wave velocity. Red indicates there are many points. The north-south direction is 0°, and the east-west direction 90°.

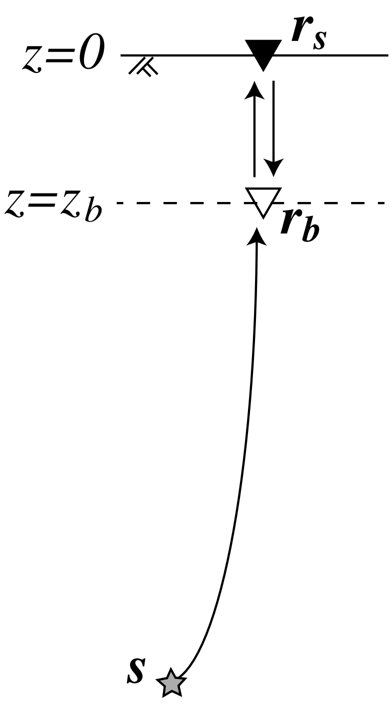

Figure A1. Geometry of an earthquake and a KiK-net station where $\boldsymbol{r_s}$ is the surface receiver (black triangle), $\boldsymbol{r_b}$ is the borehole receiver (white triangle), and $\boldsymbol{s}$ is the epicenter of earthquake (gray star).

based on the use of two independent orthogonal sources in the horizontal direction. In our study, the virtual source in the borehole has the polarization of the incident wave. The two horizontal components of the virtual source therefore are not independent, so that Alford rotation cannot be applied.

[38] The angle of the fast and slow shear wave polarization directions is 90° because we assume the incoming wave is a plane wave [*Crampin*, 1985]. A wavefield with polarization $\hat{\boldsymbol p}$, which is a unit vector, can be expressed in the polarization of the fast and slow shear waves:

$$\hat{\boldsymbol p} = \hat{\boldsymbol p}_{\boldsymbol f} \cos\phi + \hat{\boldsymbol p}_{\boldsymbol s} \sin\phi, \tag{B1}$$

where ϕ is the polarization angle in the arbitrary wavefield relative to the direction of the fast shear wave polarization, and $\hat{\boldsymbol p}_{\boldsymbol f}$ and $\hat{\boldsymbol p}_{\boldsymbol s}$ are the unit vectors of the fast and slow velocity wavefields, respectively (see Figure B1).

[39] The incoming wavefield $\boldsymbol u_b$ at the borehole receiver is

$$\boldsymbol{u_b} = S(t)\hat{\boldsymbol p} = S(t)\hat{\boldsymbol p}_{\boldsymbol f} \cos\phi + S(t)\hat{\boldsymbol p}_{\boldsymbol s} \sin\phi, \tag{B2}$$

where $S(t)$ is the incoming wavefield, and t the time. The wavefield at surface receiver $\boldsymbol u_s$ is given by

$$\boldsymbol u_s = S\left(t - \frac{z_b}{v_f}\right)\hat{\boldsymbol p}_{\boldsymbol f} \cos\phi + S\left(t - \frac{z_b}{v_s}\right)\hat{\boldsymbol p}_{\boldsymbol s} \sin\phi, \tag{B3}$$

where v_f is the fast velocity, v_s the slow velocity, and z_b the distance between the top and bottom receivers.

[40] The component of $\boldsymbol u_s$ along $\hat{\boldsymbol p}$ is

$$\begin{aligned} u_s(\phi) &= (\hat{\boldsymbol p} \cdot \boldsymbol u_s) \\ &= S\left(t - \frac{z_b}{v_f}\right)(\hat{\boldsymbol p} \cdot \hat{\boldsymbol p}_{\boldsymbol f}) \cos\phi + S\left(t - \frac{z_b}{v_s}\right)(\hat{\boldsymbol p} \cdot \hat{\boldsymbol p}_{\boldsymbol s}) \sin\phi \\ &= S\left(t - \frac{z_b}{v_f}\right) \cos^2\phi + S\left(t - \frac{z_b}{v_s}\right) \sin^2\phi. \end{aligned} \tag{B4}$$

[41] We express v_f and v_s in the average velocity v_0 and the difference δ:

$$\frac{1}{v_f} = \frac{1}{v_0} - \delta, \quad \frac{1}{v_s} = \frac{1}{v_0} + \delta, \tag{B5}$$

and assume the splitting time $z_b\delta$ is much smaller than the period. We insert expression (B5) into equation (B4) and expand using first-order Taylor expansion in δ:

$$\begin{aligned} u_s(\phi) &= S\left(t - \frac{z_b}{v_0} + z_b\delta\right)\cos^2\phi + S\left(t - \frac{z_b}{v_0} - z_b\delta\right)\sin^2\phi \\ &= S\left(t - \frac{z_b}{v_0}\right)\left(\sin^2\phi + \cos^2\phi\right) \\ &\quad + S'\left(t - \frac{z_b}{v_0}\right) z_b\delta\left(\cos^2\phi - \sin^2\phi\right) \\ &= S\left(t - \frac{z_b}{v_0}\right) + S'\left(t - \frac{z_b}{v_0}\right) z_b\delta\cos2\phi \\ &= S\left(t - \frac{z_b}{v_0} + z_b\delta\cos2\phi\right), \end{aligned} \tag{B6}$$

where S' is the time derivative of S. Thus, using Taylor expansion, we obtain the velocity for a shear wave with the polarization of equation (B1):

$$v(\phi) = \frac{v_0}{1 - v_0\delta\cos2\phi}, \tag{B7}$$

or to first order in $v_0\delta$:

$$v(\phi) = v_0(1 + v_0\delta\cos2\phi). \tag{B8}$$

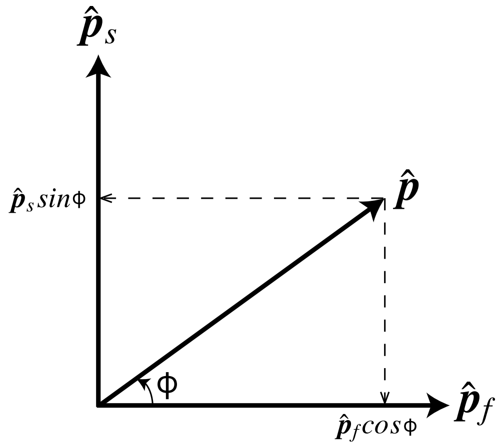

Figure B1. Projection of fast and slow velocity directions where $\hat{\boldsymbol p}_{\boldsymbol f}$ is the fast polarization direction, $\hat{\boldsymbol p}_{\boldsymbol s}$ is the slow polarization direction, $\hat{\boldsymbol p}$ is an arbitrary direction, and ϕ is the angle between the fast direction and arbitrary direction. $\hat{\boldsymbol p}$, $\hat{\boldsymbol p}_{\boldsymbol f}$, and $\hat{\boldsymbol p}_{\boldsymbol s}$ are unit vectors. Dashed arrows show the projection, which is shown in equation (B1).

Appendix C: Fourier Coefficients

[42] We describe the meaning of v_0, v_1, and v_2 in equation (5). Expression (B8) gives the velocity for a polarization ϕ relative to the polarization of the fast shear wave. When the azimuth of the fast shear wave polarization is given by ψ, the angle ϕ in equation (B8) must be changed into $\phi \rightarrow \phi - \psi$. Denoting $v_0^2\delta$ by V, these changes turn equation (B8) into

$$v(\phi) = v_0 + V\cos 2(\phi - \psi). \tag{C1}$$

This can also be written as

$$v(\phi) = v_0 + v_1\cos 2\phi + v_2\sin 2\phi; \tag{C2}$$

with

$$v_0 = \frac{1}{2\pi}\int_{-\pi}^{\pi} v(\phi)d\phi, \quad v_1 = \frac{1}{\pi}\int_{-\pi}^{\pi} v(\phi)\cos 2\phi d\phi,$$
$$v_2 = \frac{1}{\pi}\int_{-\pi}^{\pi} v(\phi)\sin 2\phi d\phi, \quad V = \sqrt{v_1^2 + v_2^2},$$
$$\psi = \frac{1}{2}\arctan\left(\frac{v_2}{v_1}\right).$$

In expression (C2), v_0, v_1, and v_2 are the Fourier coefficients of the velocity $v(\phi)$. Because v_0 does not depend on ϕ, v_0 represents the isotropic velocity. Expression (C1) shows that $v(\psi)$ and $v(\psi + \pi/2)$ are the fastest and slowest velocities, respectively. Therefore, V is the anisotropic velocity and the angle between the fast and slow polarization directions is 90°, which corresponds to shear wave splitting of a plane wave [*Crampin*, 1985].

[43] **Acknowledgments.** We are grateful to NIED for providing us with the KiK-net data and to JMA for precipitation data. We thank Diane Witters for her professional help in preparing this manuscript. We are grateful to the Assistant Editor, Kaoru Sawazaki, and one anonymous reviewer for suggestions, corrections, and discussions. Nori Nakata wants to thank for support from the Japan Society for the Promotion of Science (JSPS: 22-5857).

References

Aki, K. (1957), Space and time spectra of stationary stochastic waves, with special reference to microtremors, *Bull. Earthquake Res. Inst. Univ. Tokyo*, *35*, 415–456.

Alford, R. M. (1986), Shear data in the presence of azimuthal anisotropy: Dilley, Texas, *SEG Expanded Abstr.*, *5*, 476–479.

Bakulin, A., and R. Calvert (2004), Virtual source: New method for imaging and 4D below complex overburden, *SEG Expanded Abstr.*, *23*, 112–115.

Bakulin, A., and R. Calvert (2006), The virtual source method: Theory and case study, *Geophysics*, *71*(4), S1139–S1150.

Bakulin, A., and A. Mateeva (2008), Estimating interval shear-wave splitting from multicomponent virtual shear check shots, *Geophysics*, *73*(5), A39–A43.

Brenguier, F., M. Campillo, C. Hadziioannou, N. M. Shapiro, R. M. Nadeau, and E. Larose (2008), Postseismic relaxation along the San Andreas Fault at Parkfield from continuous seismological observations, *Science*, *321*, 1478–1481.

Chapman, D., and O. Godin (2001), Dispersion of interface waves in sediments with power-law shear speed profiles. II. Experimental observations and seismo-acoustic inversions, *J. Acoust. Soc. Am.*, *110*, 1908–1916.

Claerbout, J. F. (1968), Synthesis of a layered medium from its acoustic transmission response, *Geophysics*, *33*(2), 264–269.

Crampin, S. (1985), Evaluation of anisotropy by shear-wave splitting, *Geophysics*, *50*(1), 142–152.

Das, B. (1993), *Principles of Soil Dynamics*, PWS-Kent, Boston.

Draganov, D., K. Wapenaar, W. Mulder, J. Singer, and A. Verdel (2007), Retrieval of reflections from seismic background-noise measurements, *Geophys. Res. Lett.*, *34*, L04305, doi:10.1029/2006GL028735.

Draganov, D., X. Campman, J. Thorbecke, A. Verdel, and K. Wapenaar (2009), Reflection images from ambient seismic noise, *Geophysics*, *74*(5), A63–A67.

Hohl, D., and A. Mateeva (2006), Passive seismic reflectivity imaging with ocean-bottom cable data, *SEG Expanded Abstr.*, *25*, 1560–1564.

Larose, E., L. Margerin, A. Derode, B. van Tiggelen, M. Campillo, N. Shapiro, A. Paul, L. Stehly, and M. Ta (2006), Correlation of random wavefields: An interdisciplinary review, *Geophysics*, *71*(4), S111–S121.

Lawson, C. L. (1984), C_1 surface interpolation for scattered data on a sphere, *Rocky Mt. J. Math.*, *14*(1), 177–202.

Li, Y.-G., J. E. Vidale, K. Aki, F. Xu, and T. Burdette (1998), Evidence of shallow fault zone strengthening after the 1992 M7.5 Landers, California, earthquake, *Science*, *279*, 217–219.

Lin, F.-C., M. H. Ritzwoller, and R. Snieder (2009), Eikonal tomography: Surface wave tomography by phase front tracking across a regional broad-band seismic array, *Geophys. J. Int.*, *177*, 1091–1110, doi:10.1111/j.1365-246X.2009.04105.x.

Lobkis, O. I., and R. L. Weaver (2001), On the emergence of the Green's function in the correlations of a diffuse field, *J. Acoust. Soc. Am.*, *110*, 3011–3017.

Ma, S., G. A. Prieto, and G. C. Beroza (2008), Testing community velocity models for southern California using the ambient seismic field, *Bull. Seismol. Soc. Am.*, *98*, 2694–2714, doi:10.1785/0120080947.

Mehta, K., R. Snieder, and V. Graizer (2007a), Extraction of near-surface properties for a lossy layered medium using the propagator matrix, *Geophys. J. Int.*, *169*, 271–280.

Mehta, K., R. Snieder, and V. Graizer (2007b), Downhole receiver function: A case study, *Bull. Seismol. Soc. Am.*, *97*, 1396–1403.

Mehta, K., J. L. Sheiman, R. Snieder, and R. Calvert (2008), Strengthening the virtual-source method for time-lapse monitoring, *Geophysics*, *73*(3), S73–S80.

Minato, S., T. Matsuoka, T. Tsuji, D. Draganov, J. Hunziker, and K. Wapenaar (2011), Seismic interferometry using multidimensional deconvolution and crosscorrelation for crosswell seismic reflection data without borehole sources, *Geophysics*, *76*(1), SA19–SA34.

Miyazawa, M., R. Snieder, and A. Venkataraman (2008), Application of seismic interferometry to exptract P and S wave propagation and observation of shaear-wave splitting from noise data at Cold Lake, Alberta, Canada, *Geophysics*, *73*(4), D35–D40.

Nakajima, J., and A. Hasegawa (2004), Shear-wave polarization anisotropy and subduction-induced flow in the mantle wedge of northeastern Japan, *Earth Planet. Sci. Lett.*, *225*, 365–377.

Nakajima, J., T. Matsuzawa, A. Hasegawa, and D. Zhao (2001), Three-dimensional structure of V_p, V_s, and V_p/V_s beneath northeastern Japan: Implications for arc magmatism and fluids, *J. Geophys. Res.*, *106*, 21,843–21,857.

Nakajima, J., J. Shimizu, S. Hori, and A. Hasegawa (2006), Shear-wave splitting beneath the southwestern Kurile arc and northeastern Japan arc: A new insight into mantle return flow, *Geophys. Res. Lett.*, *33*, L05305, doi:10.1029/2005GL025053.

Nakata, N., and R. Snieder (2011), Near-surface weakening in Japan after the 2011 Tohoku-Oki earthquake, *Geophys. Res. Lett.*, *38*, L17302, doi:10.1029/2011GL048800.

Nakata, N., R. Snieder, T. Tsuji, K. Larner, and T. Matsuoka (2011), Shear-wave imaging from traffic noise using seismic interferometry by cross-coherence, *Geophysics*, in press.

Okada, T., T. Matsuzawa, and A. Hasegawa (1995), Shear-wave polarization anisotropy beneath the north-eastern part of Honshu, Japan, *Geophys. J. Int.*, *123*, 781–797.

Okada, Y., K. Kasahara, S. Hori, K. Obara, S. Sekiguchi, H. Fujiwara, and A. Yamamoto (2004), Recent progress of seismic observation networks in Japan—Hi-net, F-net, K-NET and KiK-net, *Earth Planets Space*, *56*, 15–28.

Prieto, G. A., J. F. Lawrence, and G. C. Beroza (2009), Anelastic Earth structure from the coherency of the ambient seismic field, *J. Geophys. Res.*, *114*, B07303, doi:10.1029/2008JB006067.

Roux, P., and M. Fink (2003), Green's function estimation using secondary sources in a shallow wave environment, *J. Acoust. Soc. Am.*, *113*, 1406–1416.

Ruigrok, E., X. Campman, D. Draganov, and K. Wapenaar (2010), High-resolution lithospheric imaging with seismic interferometry, *Geophys. J. Int.*, *183*, 339–357, doi:10.1111/j.1365-246X.2010.04724.x.

Sagiya, T., S. Miyazaki, and T. Tada (2000), Continuous GPS array and present-day crustal deformation of Japan, *Pure Appl. Geophys.*, *157*, 2303–2322.

Sawazaki, K., H. Sato, H. Nakahara, and T. Nishimura (2009), Time-lapse changes of seismic velocity in the shallow ground caused by strong ground motion shock of the 2000 western-Tottori earthquake, Japan, as revealed from coda deconvolution analysis, *Bull. Seismol. Soc. Am.*, *99*, 352–366.

Schaff, D. P., and G. C. Beroza (2004), Coseismic and postseismic velocity changes measured by repeating earthquakes, *J. Geophys. Res.*, *109*, B10302, doi:10.1029/2004JB003011.

Schuster, G. T., J. Yu, J. Sheng, and J. Rickett (2004), Interferometric/daylight seismic imaging, *Geophys. J. Int.*, *157*, 838–852.

Sens-Schönfelder, C., and U. Wegler (2006), Passive image interferometry and seasonal variations of seismic velocities at Merapi Volcano, Indonesia, *Geophys. Res. Lett.*, *33*, L21302, doi:10.1029/2006GL027797.

Shiomi, K., K. Obara, S. Aoi, and K. Kasahara (2003), Estimation on the azimuth of the Hi-net and KiK-net borehole seismometers (in Japanese), *Zishin2*, *56*, 99–110.

Snieder, R., and E. Şafak (2006), Extracting the building response using seismic interferometry: Theory and application to the Millikan library in Pasadena, California, *Bull. Seismol. Soc. Am.*, *96*, 586–598.

Snieder, R., and A. van den Beukel (2004), The liquefaction cycle and the role of drainage in liquefaction, *Granular Matter*, *6*, 1–9, doi:10.1007/s10035-003-0151-9.

Snieder, R., K. Wapenaar, and K. Larner (2006), Spurious multiples in seismic interferometry of primaries, *Geophysics*, *71*(4), SI111–SI124.

Stehly, L., M. Campillo, B. Froment, and R. L. Weaver (2008), Reconstruction Green's function by correlation of the coda of the correlation (C_3) of ambient seismic noise, *J. Geophys. Res.*, *113*, B11306, doi:10.1029/2008JB005693.

Thomsen, L. (1988), Reflection seismology over azimuthally anisotropic media, *Geophysics*, *53*(3), 304–313.

Tonegawa, T., K. Nishida, T. Watanabe, and K. Shiomi (2009), Seismic interferometry of teleseismic S-wave coda retrieval of body waves: An application to the Philippine Sea slab underneath the Japanese Islands, *Geophys. J. Int.*, *178*, 1574–1586, doi:10.1111/j.1365-246X.2009.04249.x.

Trampert, J., M. Cara, and M. Frogneux (1993), SH propagator matrix and Q_s estimates from borehole- and surface- recorded earthquake data, *Geophys. J. Int.*, *112*, 290–299.

Vasconcelos, I., and R. Snieder (2008), Interferometry by deconvolution: Part 2. Theory for elastic waves and application to drill-bit seismic imaging, *Geophysics*, *73*(3), S129–S141.

Vidale, J. E., and Y.-G. Li (2003), Damage to the shallow Landers fault from the nearby Hector Mine earthquake, *Nature*, *421*, 524–526.

Wapenaar, K. (2004), Retrieving the elastodynamic Green's function of an arbitrary inhomogeneous medium by cross correlation, *Phys. Rev. Lett.*, *93*, 254–301.

Wapenaar, K., and J. Fokkema (2006), Green's function representations for seismic interferometry, *Geophysics*, *71*(4), SI33–SI46.

Wapenaar, K., J. van der Neut, and E. Ruigrok (2008), Passive seismic interferometry by multidimensional deconvolution, *Geophysics*, *73*(6), A51–A56.

Wapenaar, K., D. Draganov, R. Snieder, X. Campman, and A. Verdel (2010), Tutorial on seismic interferometry: Part 1. Basic principles and applications, *Geophysics*, *75*(5), 75A195–75A209.

Wegler, U., and C. Sens-Schönfelder (2007), Fault zone monitoring with passive image interferometry, *Geophys. J. Int.*, *168*, 1029–1033.

Wegler, U., H. Nakahara, C. Sens-Schönfelder, M. Korn, and K. Shiomi (2009), Sudden drop of seismic velocity after the 2004 M_w 6.6 mid-Niigata earthquake, Japan, observed with passive image interferometry, *J. Geophys. Res.*, *114*, B06305, doi:10.1029/2008JB005869.

Wu, C., Z. Peng, and D. Assimaki (2009), Temporal changes in site response associated with the strong ground motion of the 2004 M_W 6.6 Mid-Niigata earthquake sequences in Japan, *Bull. Seismol. Soc. Am.*, *99*, 3487–3495.

Yamada, M., J. Mori, and S. Ohmi (2010), Temporal changes of subsurface velocities during strong shaking as seen from seismic interferometry, *J. Geophys. Res.*, *115*, B03302, doi:10.1029/2009JB006567.

N. Nakata and R. Snieder, Center for Wave Phenomena, Department of Geophysics, Colorado School of Mines, 1500 Illinois St., Golden, CO 80401, USA. (nnakata@mines.edu)